https://doi.org/10.5194/tc-2019-250
Preprint. Discussion started: 27 November 2019

The Cryosphere Discussions
Open Access
EGU

CryoSat Ice Baseline-D Validation and Evolutions

Marco Meloni[a], Jerome Bouffard[b], Tommaso Parrinello[b], Geoffrey Dawson[c], Florent Garnier[d], Veit Helm[f], Alessandro Di Bella[e], Stefan Hendricks[f], Robert Ricker[f], Erica Webb[g], Ben Wright[g], Karina Nielsen[e], Sanggyun Lee[i], Marcello Passaro[j], Michele Scagliola[h], Sebastian Bjerregaard Simonsen[e], Louise Sandberg Sørensen[e], David Brockley[i], Steven Baker[i], Sara Fleury[d], Jonathan Bamber[c], Luca Maestri[h], Henriette Skourup[e], Rene' Forsberg[e], LorettaMizzi[k]

a. Serco c/o ESA, Earth Observation Directorate, Via Galileo Galilei, 2 –00044 Frascati, Italy;
b. ESA (European Space Agency), Earth Observation Directorate, Via Galileo Galilei, 2 – 00044 Frascati, Italy;
c. Bristol Glaciology Centre, School of Geographical Sciences, University of Bristol, Bristol, UK;
d. LEGOS, University of Toulouse, CNRS, IRD, CNES, UPS, (Toulouse), France;
e. DTU Space, National Space Institute, Department of Geodynamics, Technical University of Denmark, Kongens Lyngby, Denmark;
f. Alfred Wegener Institute, Helmholtz Centre for Polar and Marine Research Klussmanstr. 3D, 27570 Bremerhaven, Germany;
g. Telespazio VEGA UK Ltd., 350 Capability Green, Luton, Bedfordshire LU1 3LU, UK;
h. Aresys S.r.l., via Privata Flumendosa, 16, 20132, Milan, Italy;
i. University College London at The Mullard Space Science Laboratory, Holmbury St Mary, RH5 6NT, UK;
j. Deutsches Geodatisches Forschungsinstitut (DGFI/TUM), Munchen, Germany;
k. Telespazio, Via Tiburtina, 965, 00156 Rome, Italy.

Corresponding Author: Meloni, M., marco.meloni@esa.int

https://doi.org/10.5194/tc-2019-250
Preprint. Discussion started: 27 November 2019

The Cryosphere Discussions
Open Access
EGU

Abstract

The ESA Earth Explorer CryoSat-2 was launched on 8 April 2010 to monitor the precise changes in the thickness of terrestrial ice sheets and marine floating ice. For that, CryoSat orbits the planet at an altitude of around 720 km with a retrograde orbit inclination of 92 ° and a ‘‘quasi” repeat cycle of 369 days (30 days sub-cycle). To reach the mission goals, the CryoSat products have to meet the highest quality standards to date, achieved through continual improvements of the operational processing chains. The new CryoSat Ice Baseline-D, in operation since 27th May 2019, represents a major processor upgrade with respect to the previous Ice Baseline-C. Over land ice the new Baseline-D provides better results with respect to previous baseline when comparing the data to a reference elevation model over the Austfonna ice cap region, improving the ascending and descending crossover statistics from 1.9 m to 0.1 m. The improved processing of the star tracker measurements implemented in Baseline-D has led to a reduction of the standard deviation of the point-to-point comparison with the previous star tracker processing method implemented in Baseline-C from 3.8 m to 3.7 m. Over sea ice, the Baseline-D improves the quality of the retrieved heights in areas up to ~12 km inside the Synthetic Aperture Radar Interferometric (SARIn or SIN) acquisition mask, which is beneficial not only for freeboard retrieval, but for any application that exploits the phase information from SARIn Level-1 (L1) products. In addition, scatter comparisons with the Beaufort Gyre Exploration Project (BGEP, https://www.whoi.edu/beaufortgyre) and Operation IceBridge (OIB, Kurtz et al., 2013) in-situ measurements confirm the improvements in the Baseline-D freeboard product quality. Relative to OIB, the Baseline-D freeboard mean bias is reduced by about 8 cm, which roughly corresponds to a 60% decrease with respect to Baseline-C. The BGEP data indicate a similar tendency with a mean draft bias lowered from 0.85 m to -0.14 m. For the two in-situ datasets, the Root Mean Square Deviation (RMSD) is also well reduced from 14 cm to 11 cm for OIB and with a factor 2 for BGEP. Observations

https://doi.org/10.5194/tc-2019-250
Preprint. Discussion started: 27 November 2019

51 over inland waters, show a slight increase in the percentage of "good observations" in Baseline-
52 D, generally around 5-10 % for most lakes. This paper provides an overview of the new Level-
53 1 and Level-2 (L2) CryoSat ice Baseline-D evolutions and related data quality assessment,
54 based on results obtained from analysing the 6-month Baseline-D test dataset released to
55 CryoSat expert users prior the final transfer to operations.

56

57 **Keywords:** CryoSat; Altimetry; Cryosphere; Ice product status; Instrument performance;
58 Long-term stability; Ice product evolutions

59

60

61

62

63

64

65

66

67

68

69

https://doi.org/10.5194/tc-2019-250
Preprint. Discussion started: 27 November 2019


The Cryosphere
Discussions
Open Access
EGU

1 Introduction

To better understand how climate change is affecting the Polar Regions in terms of diminishing ice cover as a consequence of global warming, it remains an urgent need to determine more precisely how the thickness of the ice is changing, both on land and floating on the sea, as also detailed in the last IPCC special report on Ocean and Cryosphere (https://www.ipcc.ch/srocc/download-report/).

In this respect, the ESA Earth Explorer CryoSat-2 (hereafter CryoSat), monitors the changes in the thickness of marine ice floating in the polar oceans and of the variations in the thickness of vast ice sheets which are contributing to global sea level rise. To achieve its primary mission objectives, the CryoSat altimeter is characterised by three operating modes, which are activated according to a geographic mode mask: 1) pulse width limited Low Resolution Mode (LRM), 2) pulse width limited and phase coherent single channel Synthetic Aperture Radar (SAR) mode and 3) the dual channel pulse width and phase coherent Synthetic Aperture Radar interferometric (SARIn) mode.

The CryoSat data are operationally processed by ESA over both ice and ocean surfaces using two independent processors (ice and ocean), generating a range of operational products with specific latencies. The ice processor generates Level 1B (L1B) and Level 2 (L2) offline products typically 30 days after data acquisition for the three instrument modes: LRM, SAR and SARIn. The ice products are currently generated with the Ice Baseline-D processors. In addition, Near Real Time (NRT) products are also generated with a latency of 2-3 hours after sensing to support forecasting services. Details on the previous historic CryoSat ice processing chain and main L1B and L2 processing steps are reported in Bouffard et al., 2018b. CryoSat ocean products are instead generated with the Baseline-C CryoSat Ocean Processor (more details in Bouffard et al., 2018a). An overview of the current CryoSat data products is reported in Figure 1.

https://doi.org/10.5194/tc-2019-250
Preprint. Discussion started: 27 November 2019

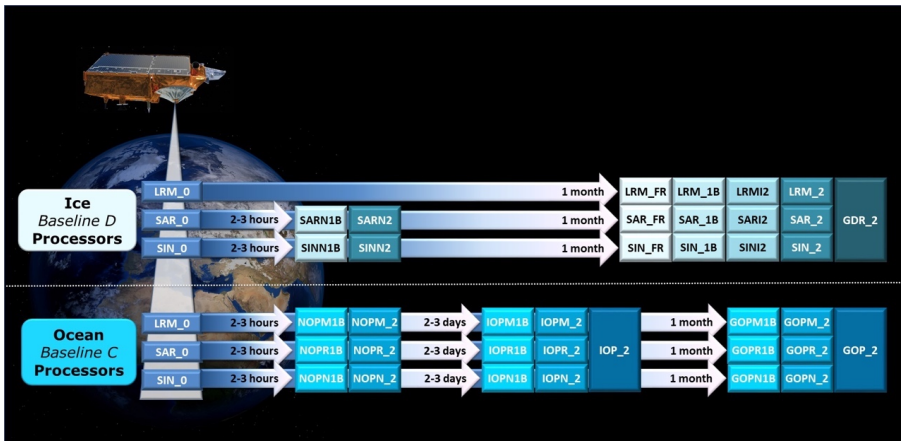

Figure 1 CryoSat Data Products overview. Map Data ©2019 Google

In order to achieve the highest quality of data products, and meet mission requirements, the CryoSat Ice and Ocean processing chains are periodically updated. Processing algorithms and associated product content are regularly improved based on recommendations from the scientific community, Expert Support Laboratories, Quality Control Centres and validation campaigns. In this regard, the new CryoSat Ice Baseline-D processors have been developed and tested. An Ice Baseline-D Test Data Set (TDS) covering three different time periods (September - November 2013, February - April 2014 and April 2016 (only SARIn)) was made available to the CryoSat Quality Working Group (QWG) and scientific experts in order to opportunely validate and quality check the new products. This paper provides an overview of the CryoSat Ice Baseline-D evolutions of the processing algorithms and focuses on the in-depth validation performed on the TDS over land ice, sea ice and inland waters domains. The transfer to operations of the new CryoSat Ice Baseline-D processors was performed on 27th May 2019 and a complete mission data reprocessing is on-going in order to provide users with homogeneous and coherent CryoSat ice products for proper data exploitation and analysis.

The paper is structured as follows. Section 2 provides an extensive analysis of the major evolutions included in the Baseline-D separated between L1B and L2 processing stages,

https://doi.org/10.5194/tc-2019-250
Preprint. Discussion started: 27 November 2019

112 describing the improvements that have been implemented and included in the new baseline
113 version. Section 3 describes, based on the analysis of the 6-month TDS provided by ESA, the
114 main validation results in different domains such as land ice, sea ice and inland waters. Section
115 4 reports the conclusions.
116
117
118

https://doi.org/10.5194/tc-2019-250
Preprint. Discussion started: 27 November 2019

2 CryoSat Ice Baseline-D Evolutions

The new Ice Baseline-D processors were approved and transferred to operation on 27th May 2019. A complete list of the evolutions and changes implemented in Baseline-D can be found in the technical note available at https://earth.esa.int/documents/10174/125272/CryoSat-Baseline-D-Evolutions while a concise overview of the CryoSat L1B and L2 ice products is available at https://earth.esa.int/documents/10174/125272/CryoSat-Baseline-D-Product-Handbook. This revision of the document has been released to accompany the delivery of Baseline-D CryoSat products. Details about CryoSat and main changes are described below separated between the L1B and L2 processing stages.

2.1 Ice Baseline-D L1B Evolutions

Prior to Baseline-D, the Ice Baseline-C processors were installed on the operational and reprocessing platforms and Baseline-C L1B products were produced and distributed to users since the 1st of April 2015 (Scagliola and Fornari, 2015). During this period some issues were identified and the scientific community suggested a series of evolutions that have been taken into consideration when updating the L1B processors at Baseline-D. L1B products are now generated using the new Baseline-D L1B processors, in which software issues have been fixed and new processing algorithms have been implemented (for more details refer to the Baseline-D products evolutions document available at https://earth.esa.int/documents/10174/125272/CryoSat-Baseline-D-Evolutions). One of the main quality improvements implemented at Baseline-D is the migration from Earth Explorer Format (EEF) to Network Common Data Form (NetCDF). In addition, it has been shown that the phase information available in the CryoSat SARIn acquisition mode can be used to reduce the uncertainty affecting sea ice freeboard retrievals (Armitage et al., 2014). The previous Baseline-C has shown large negative freeboard estimates at the boundary of the SARIn

https://doi.org/10.5194/tc-2019-250
Preprint. Discussion started: 27 November 2019

143 acquisition mask, caused by a bad phase difference calibration. In Baseline-D the accuracy of
144 the phase difference has been improved as well as the quality of the freeboard at the SARIn
145 boundaries, reducing drastically the percentage of negative retrievals from 25.8% to 0.8% (Di
146 Bella et al., 2019). In SAR altimetry processing, after the beam forming process, stacks are
147 formed. A stack is the collection of all the beams that have illuminated the same Doppler cell
148 (as described in http://www.altimetry.info/filestorage/Radar_Altimetry_Tutorial.pdf). At
149 Baseline-D, two additional stack characterisation parameters (also known as Beam Behaviour
150 Parameters) have been added to the SAR/SARIn L1B products. The stack peakiness (Passaro
151 et al., 2018) can be useful to improve the sea ice discrimination, and the position of the centre
152 of the Gaussian that fits the range integrated power of the single look echoes within a stack as
153 function of the look angle (Scagliola et al., 2015). In radar altimetry, the window delay refers
154 to the 2-way time between the pulse emission and the reference point at the centre of the range
155 window. The window delay in Baseline-D L1B products now compensates for the Ultra Stable
156 Oscillator (USO) correction, which is the deviation of the frequency clock of the USO from
157 the nominal frequency. The L1B users no longer need to apply this correction. In addition, the
158 accuracy of the mispointing angles has increased by properly considering in their computation
159 the so called "aberration correction" (more details in Scagliola et al., 2018).
160

161 **2.2 Ice Baseline-D L2 Evolutions**

162 The Baseline-D update to the CryoSat L2 processing fixes a number of anomalies and
163 introduces several processing algorithm improvements, as described in
164 https://earth.esa.int/documents/10174/125272/CryoSat-Baseline-D-Evolutions. In addition to
165 corrections and improvements, the L2 products are now generated in netCDF format and
166 contain all previous parameters as well as some new ones. For example, in previous baselines,
167 the freeboard sea ice processing was restricted to SAR mode regions, resulting in large gaps in

https://doi.org/10.5194/tc-2019-250
Preprint. Discussion started: 27 November 2019

coverage around the coast and in other regions of the Arctic region operating in SARIn. In Baseline D, the sea ice parameters are also computed over these regions. The height value is still that from the SARIn mode specific retracking, but new fields have been added to contain the sea ice processing height result, and freeboard and sea level anomalies are now computed in SARIn mode (previously SAR mode only). In addition, a new retracker is used for retracking diffuse waveforms from sea ice regions, and for all waveforms in non-polar regions (more details in the CryoSat Design Summary Document available at https://earth.esa.int/documents/10174/125272/CryoSat-L2-Design-Summary-Document).

Over sea ice, the discrimination algorithm used to determine if individual records represent sea ice floes, leads in the sea ice, or ice-free ocean has been improved with the implementation of a new discrimination metric based on the peakiness of the stack of SAR beam waveforms. This method, improves the capability of the algorithm to reject waveforms contaminated by off-nadir specular reflections (as described in https://earth.esa.int/documents/10174/125272/CryoSat-L2-Design-Summary-Document).

Some tuning of the thresholds for the other metrics has also been performed, based on analysis of the test datasets. For the land ice domain, new slope models have been generated, using the Digital Elevation Models (DEMs) of Antarctica and Greenland described in Helm et al. (2014). These models were created with more recently acquired data and therefore better represent the slope of the surface during the period of the CryoSat mission. The DEMs were sampled at high resolution to derive the surface slope to make the correction more responsive to changes in slope. Lastly, several improvements have been made to the contents of the L2 products. The surface type mask model used to discriminate different types of targets, has been updated (as described in the Baseline-D product handbook available at https://earth.esa.int/documents/10174/125272/CryoSat-Baseline-D-Product-Handbook).

Variables have been added to the netCDF to explicitly cross-reference the 1 Hz and 20 Hz data.

https://doi.org/10.5194/tc-2019-250
Preprint. Discussion started: 27 November 2019

193 Finally, the retracker-corrected range to the surface has been added to the product (in addition
194 to the height).
195

https://doi.org/10.5194/tc-2019-250
Preprint. Discussion started: 27 November 2019

196 **3 CryoSat Ice Baseline-D Validation of Test Dataset Results**

197 **3.1 Data Quality: Ice Baseline-D Test Data Verification by IDEAS+**

198 All CryoSat data products are routinely monitored for quality control by the ESA/ESRIN
199 Sensor Performance, Products and Algorithms (SPPA) office with the support of the Instrument
200 Data quality Evaluation and Analysis Service (IDEAS+). In preparation for the Ice Baseline-
201 D, IDEAS+ performed Quality Control (QC) checks on test data generated with the new Ice
202 Baseline-D processors (IPF1 vN1.0 & IPF2 vN1.0). For testing and validation purposes a 6-
203 month TDS was generated at ESA on a dedicated processing environment for two periods:
204 September – November 2013; February – April 2014. IDEAS+ performed QC of a 10-day
205 sample of L1B and L2 data, to assess data quality and check for major anomalies. Following
206 this QC checks, this 6-month TDS was made available to the CryoSat QWG for more detailed
207 scientific analysis.
208 The content of the product header files (.HDR) was checked to confirm that all Data Set
209 Descriptors (DSDs) were present and correct and all header fields were correctly filled.
210 Similarly, the global attributes section of the netCDF has been checked to ensure data files was
211 consistent and complete. The test Baseline-D products were also checked for any unexpected
212 flags, that may indicate processing anomalies, and all external geophysical corrections were
213 checked to ensure that they were computed correctly. Some minor unexpected changes to the
214 configuration of particular flags was observed as well as the incorrect scaling of the altimeter
215 wind speed values. These minor issues have been resolved in the final Baseline-D release,
216 which has been implemented into operations.
217
218
219

https://doi.org/10.5194/tc-2019-250
Preprint. Discussion started: 27 November 2019

220 ## 3.2 Land Ice

221 ### 3.2.1 Impact of algorithm evolution on land ice products

222 CryoSat L1B and L2 products generated using the Baseline-C are the primary input to obtain
223 elevation change time series of the large ice sheets. As those time series are the primary data
224 set to obtain ice sheet wide mass balance and therefore the contribution to sea level change, a
225 consistent high quality CryoSat L1B/2 product is essential. To derive mass balance estimates
226 the Alfred Wegener Institute (AWI) processing chain was used, introduced by Helm et. al.
227 2014, including TFMRA (Threshold First-Maximum Retracker Algorithm) re-tracking and the
228 refined slope correction (Roemer, et. al., 2007) for LRM mode as well as an interferometric
229 processing using phase and coherence for the SARIn mode L1B data products. In addition,
230 several other groups rely on high quality L1B and L2 data products to generate time series of
231 elevation, respectively mass change (e.g. Nilsson et al., 2015; Simonsen et al, 2017; McMillan
232 et al., 2014; Schroeder et al, 2019). Next to the conventional along track processing, the swath
233 mode has been developed and explored by several groups (Gray et al., 2013; Gourmelen et al.,
234 2017). It has been demonstrated that swath products can be used to estimate basal melt rates of
235 ice shelves (Gourmelen et al., 2017) or high-resolution elevation change time series within the
236 steep margins of the Greenland ice sheet or Arctic Ice Caps. However, a small attitude angle
237 error interpreted as a mispointing error has been observed, which is critical for the accuracy of
238 swath mode products. Bouffard et al., 2018b presented an attitude correction to be applied to
239 Baseline-C products, which should help to reduce this uncertainty. To estimate the impact of
240 the algorithm evolution of the CryoSat Ice Processor to Baseline-D on land ice data records,
241 L2 type products for Baseline-C and Baseline-D were compute using the AWI processing
242 chain. In addition, Level 2 “In-depth” (L2I) product retracker and slope corrections were
243 implemented in the individual data sets to be compared. In a first instance single tracks crossing
244 the Antarctic ice sheet were compared on a point to point basis for all of the individual

https://doi.org/10.5194/tc-2019-250
Preprint. Discussion started: 27 November 2019

245 parameters included in the L1B and L2I products. Most of the parameters were found to show
246 close agreement, however a constant offset was found for sigma0 for all of the implemented
247 LRM L2 retrackers: 0.6 dB, 0.63 dB, 0.65 dB for Ocean, Ice1, Ice2 retracker respectively. This
248 needs to be considered, as long as both Baselines are used in combination to estimate elevation
249 change time series, as some groups incorporate a sigma0 correlated correction. Furthermore,
250 Baseline-D uses an updated surface type mask. This has significantly improved in the ice shelf
251 area around Antarctica, as shown in Figure 2 for the Filchner-Ronne ice shelf.

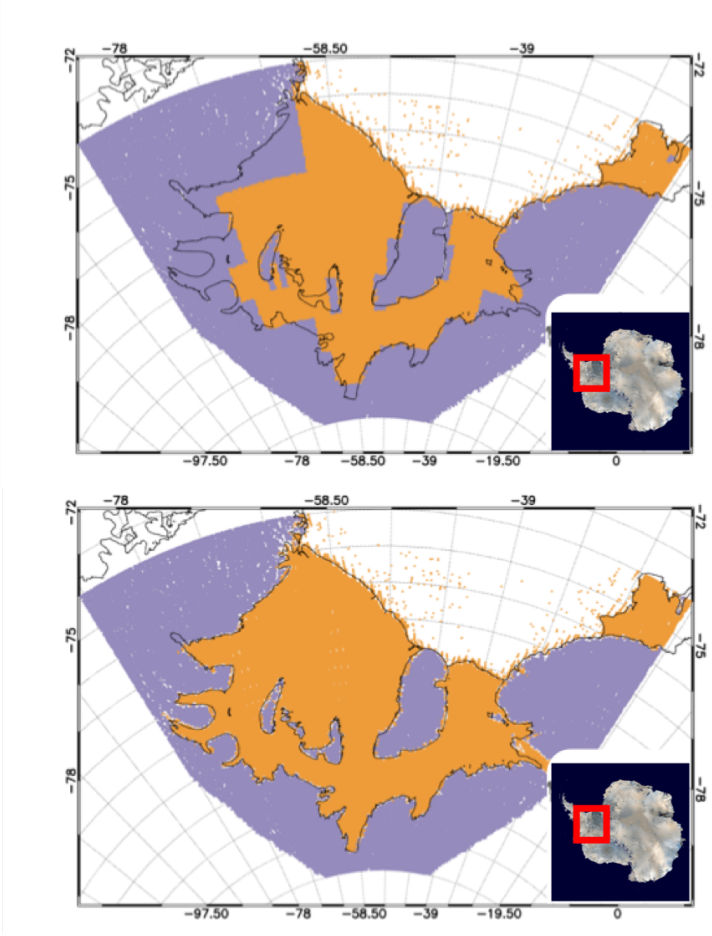

252

Figure 2 Surface Type mask shown for the Filchner Ronne ice shelve area. Upper panel Baseline-C; Lower panel Baseline-D. Map Data ©NASA/Dave Pape

https://doi.org/10.5194/tc-2019-250
Preprint. Discussion started: 27 November 2019

253 Now, this mask can be applied to differentiate between floating and grounded ice. In addition,
254 a new slope model for Antarctica, which is based on the elevation model of Helm et al., 2014,
255 is implemented in Baseline-D. This slightly changes the LRM slope corrected elevation as is
256 demonstrated for a large area in East Antarctica in Figure 3.

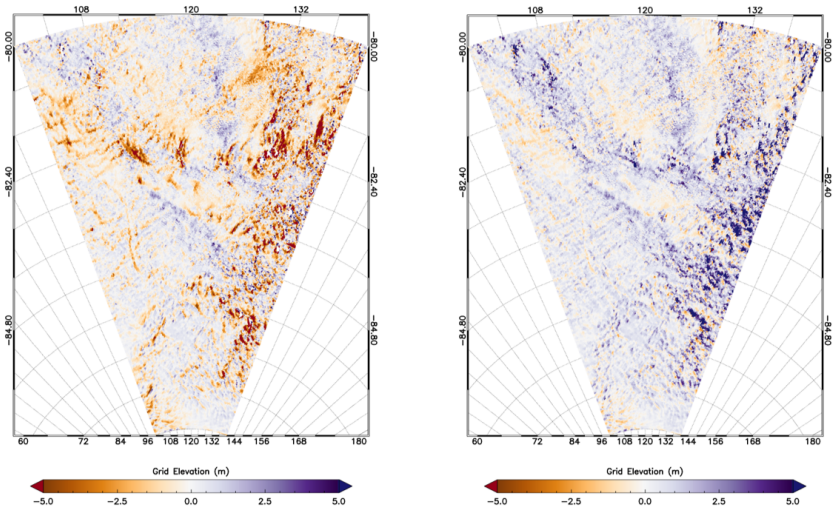

257

Figure 3 Differences of slope corrected LRM data to reference DEM (REMA) in East Antarctica.

Left: Baseline-C: +0.13 +/- 1.2m, right Baseline-D: -0.11 +/- 1.11 m

258 Differences to an independent Antarctic elevation model (REMA) are shown for both
259 Baselines. The differences vary spatially and the overall mean changed from +0.13 m to -0.11
260 m. This needs to be considered when estimating time series using data both Baselines, until the
261 full mission reprocessing is finished. The attitude information for SARIn, such as Roll, Pitch
262 and Yaw were updated for Baseline-D, incorporating the correction found by Bouffard at al.,
263 2018b. The correction is as expected and agrees with the auxiliary product already delivered
264 by ESA. This has negligible effect for SARIn Point Of Closest Approach (POCA) elevations,
265 however major improvements for swath processed data as shown in Figure 4 and Figure 5.
266 Figure 4 subpanels show the difference of swath processed data for ascending and descending

https://doi.org/10.5194/tc-2019-250
Preprint. Discussion started: 27 November 2019

267 tracks to a reference elevation model derived from TanDEM-X data from 2012 for the
268 Austfonna icecap, respectively. The large positive anomaly is a known glacier surge event
269 (McMillan et al., 2014). The negative anomaly observed by descending tracks in the eastern
270 part and the discrepancy between ascending and descending tracks in the western part in
271 Baseline-C (subpanel B) could be reduced. More clearly, Figure 5 shows this improvement in
272 the crossover statistics. With the upcoming Baseline-D a correction term as suggested by Gray
273 et al., 2017, is not needed any more and might not be appropriate as a static correction to
274 Baseline-C, as the angle correction is variable in space and time.

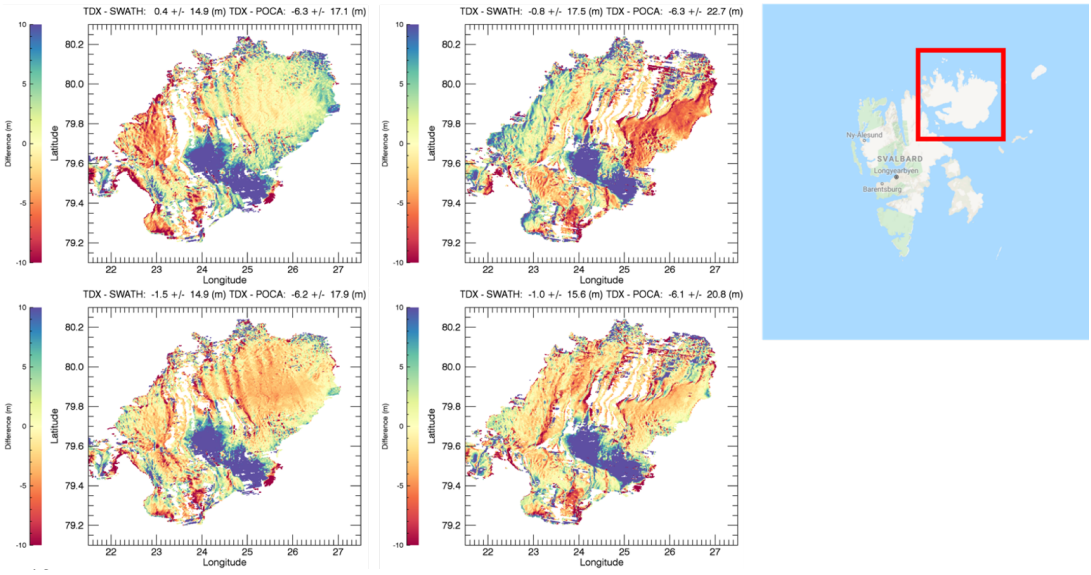

Figure 4 Differences to reference elevation model derived from TanDEM-X data from 2012 across the Austfonna ice cap. Upper left: ascending Baseline-C, Upper right: descending Baseline-C, Lower left: ascending Baseline-D, Lower right: descending Baseline-D. Map Data ©2019 Google

276

277

https://doi.org/10.5194/tc-2019-250
Preprint. Discussion started: 27 November 2019

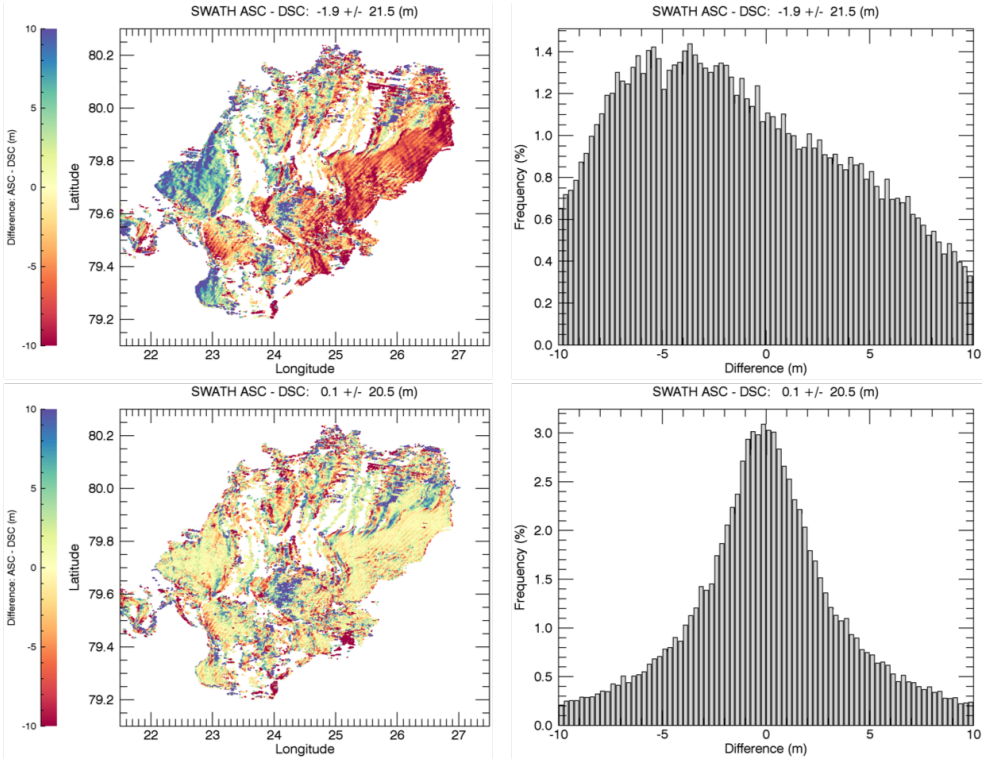

Figure 5 Crossovers between ascending and descending swath data across Austfonna ice cap. Upper panels: Baseline-C + statistics. Lower panels: Baseline-D + statistics

3.2.2 Baseline-D SARIn swath data over Antarctica

Standard radar altimetry relies on the determination of the Point Of Closest Approach (POCA), sampling a single elevation beneath the satellite. Using CryoSat's interferometric mode (SARIn), it is possible to resolve more than just the elevation at the POCA. If the ground terrain slope is only a few degrees, the CryoSat altimeter operates in a manner such that the interferometric phase of the altimeter echoes may be unwrapped to produce a wide swath of elevation measurements across the satellite ground track beyond the POCA. Swath processing also provides a near continuous elevation field, making it possible to form digital elevation models and to map rates of surface elevation change at a true resolution of 500 m, an order of magnitude finer than is the current state of the art for the continental ice sheets (Gourmelen et

https://doi.org/10.5194/tc-2019-250
Preprint. Discussion started: 27 November 2019

al., 2018). To assess the performance of swath data derived from Baseline-C and Baseline-D CryoSat L1B data, a point-to-point comparison was performed over the Siple Dome, Antarctica. This comparison gave a measure of the precision of swath elevation measurement and allowed for a comparison of each Baseline. The Siple Dome region has been chosen as it is a relatively stable area with large areas of constant sloping terrain, ensuring a high sampling density of swath data.

The Baseline-D TDS from February – April 2014 and the Baseline-C data from the same time period were used in this assessment. Baseline-C data were used with both the original star tracker measurements and with revised measurements provided by ESA. These were supplied as a result of an incorrect mispointing angle for the aberration of light being implemented in Baseline-C, which led to an error in the calculation of the roll of the satellite. Any error in the roll will result in an error in the geolocation and derived height, and this was shown to decrease the performance of swath measurements (Gray et al., 2017). Swath data were processed following Gray et al., 2013, with a minimum coherence and power threshold of 0.9 and -180 dB respectively. For the point-to-point comparison, the closest individual swath elevation measurement from a different satellite pass was used. A comparison was only made if the maximum distance between the two geolocated elevation measurement was below 30 m. Overall 157,000 points were compared at an average distance of 19 m. As the points compared were distributed over sloping terrain, any difference in position lead to an additional error, for example a horizontal offset of 19 m over a 0.5 degree slope lead to a vertical offset of ~0.17 m which is included in all comparisons. The standard deviation between the point-to-point comparison for Baseline-C with the original (Figure 6a) and the revised star tracker measurements (Figure 6b) was 4.2 m and 3.8 m respectively, showing that correcting for the mispointing angle for aberration of light error significantly improves the precision of swath measurements. While the standard deviation of the point-to-point comparison for Baseline-D

https://doi.org/10.5194/tc-2019-250
Preprint. Discussion started: 27 November 2019

315 was 3.7 m, showing a slight improvement compared to Baseline-C, which can be attributed to
316 improved processing of the star tracker measurements documented in Baseline-D.

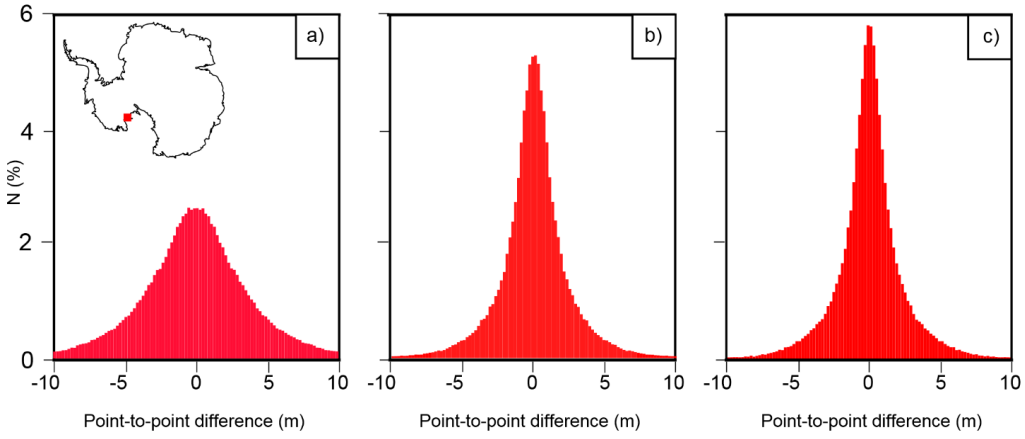

317

Figure 6 Point-to-point comparison of swath data over the Siple Dome (red box in map insert) for (a) Baseline-C with original star tracker measurements (b) Baseline-C with revised star tracker measurements and (c) Baseline-D.

318

319 ### 3.2.3 SARIn Validation at Austfonna, Svalbard

320 The Southeastern basin of the Austfonna ice cap, Svalbard, began surging in 2012 (Dunse et
321 al. 2012; Dunse et al. 2015). The surge resulted in a heavily crevassed surface of the basin,
322 creating a challenging surface topography for radar altimetry. CryoSat operates in the new and
323 innovative SARIn mode over the Austfonna ice cap and due to the complex surface, the ice
324 cap has been chosen as a primary validation site for the CryoSat mission in the ESA CryoSat
325 Validation Experiment (CryoVEx) and the ESA CryoVal-Land Ice (LI) projects. Based on
326 recommendations from the ESA project, CryoVal-LI, the 2016 CryoVEx airborne campaign
327 (Skourup et al. 2018) revised the traditional satellite under-flights to fly parallel lines with
328 spacing of 1 or 2 km next to the CryoSat nadir-ground tracks. Sandberg Sørensen et al. 2018
329 used airborne laser scanning (ALS) data collected at Austfonna in 2016 to validate the data
330 gathered by CryoSat in April 2016, and processed by six dedicated retrackers. We refer the

https://doi.org/10.5194/tc-2019-250
Preprint. Discussion started: 27 November 2019

reader to Sandberg Sørensen et al. 2018 for a detailed description of the applied retrackers and schematics of the validation procedure. The six retrackers available in the original study were: (1) ESA Baseline-C L2 retracker (https://earth.esa.int/documents/10174/125272/CryoSat-Baseline-C-Ocean-Product-Handbook); (2 and 3) The AWI land ice processing, with and without the use of a digital elevation model (AWI and AWI DEM, (Helm et al. 2014)); (4) The NASA Jet Propulsion Lab land ice CryoSat processing (JPL, (Nilsson et al. 2016)); (5) The Technical University of Denmark (DTU) Advanced Retracking System (LARS NPP50, (Villadsen et al. 2015)); and (6) University of Ottawa (UoO) CryoSat processing (Gray et al. 2013; Gray et al. 2015; Gray et al. 2017)). All retrackers were applied to the ESA Baseline-C L1 waveforms.

The geolocation of the SARIn echo is dependent on the phase at the retracking point hence the geolocated heights, based on different retracker, cannot be directly compared. Sandberg Sørensen et al., 2018 relied on comparing the precise geolocation of the ALS with the individual observations from each retracker, and then provided the derived statistics for all ALS-CS2 crossovers and for the subset of common nadir position for all retrackers. As the number of common nadir positions will change if new retrackers are added to the study, Sandberg Sørensen et al. 2018 also provide the validation code as supplementary material to the publication. Potentially, this code can be used as a benchmark for future retracker development. Here, we add the April 2016 Baseline-D ice TDS in benchmarking the code to pinpoint the differences (Figure 7) and highlight improvement in the new Baseline-D. Table 1 provides the updated statistics, (comparable with Table 1 in Sandberg Sørensen et al. 2018). The addition of the Baseline-D data reduced the number of common nadir positions from 600 to 497. However, when Baseline-C and D solutions are compared, the new baseline improves the agreement with the ALS observations in Area 2. The results are more mixed in Area 3 where the surface is rougher and heavily crevassed due to the surging behaviour of this area.

https://doi.org/10.5194/tc-2019-250
Preprint. Discussion started: 27 November 2019

356 However, there is still room for improvement before the dedicated land ice retrackers of AWI,

357 JPL and UoO are reached.

Table 1: Updated statistics for Sandberg Sørensen et al. 2018, with the inclusion of the new ESA Baseline-D L2 processing of CryoSat. The improvements of the new processing are especially noticeable in the standard deviation (Std. dev) of observations in Area 2 (see Figure 7).

Area	CS2 Data Set	ESA C	ESA D	JPL	AWI (DEM)	AWI	LARS	UoO
1	# of ΔH	777 (497)	774 (497)	725 (497)	787 (497)	828 (497)	768 (497)	752 (497)
	Mean [m]	2.80 (3.89)	2.23 (3.83)	1.14 (-0.06)	4.65 (3.68)	4.42 (4.69)	13.64 (15.45)	0.93 (0.53)
	Median [m]	-1.11 (-1.21)	-1.28 (-1.32)	-0.28 (-0.34)	2.04 (1.99)	2.34 (2.28)	5.53 (5.28)	-0.31 (-0.58)
	Std. Dev. [m]	30.28 (33.60)	28.58 (34.29)	11.71 (3.58)	11.84 (6.59)	18.45 (18.37)	43.52 (49.49)	4.80 (4.53)
2	# of ΔH	509 (335)	507 (335)	470 (335)	509 (335)	512 (335)	494 (335)	497 (335)
	Mean [m]	-0.76 (-1.40)	-1.54 (-1.69)	-0.48 (-0.49)	4.31 (1.53)	2.72 (2.29)	4.89 (3.84)	-0.56 (-0.76)
	Median [m]	-1.04 (-1.07)	-1.24 (-1.26)	-0.34 (-0.52)	1.63 (1.98)	2.04 (1.98)	5.53 (5.01)	-0.97 (-1.10)
	Std. Dev. [m]	14.63 (3.18)	4.49 (3.34)	2.93 (1.84)	12.57 (1.98)	6.61 (1.98)	19.19 (21.4)	1.97 (1.83)
3	# of ΔH	268 (149)	267 (149)	258 (149)	278 (149)	318 (149)	274 (149)	256 (149)
	Mean [m]	9.57 (16.23)	9.39 (16.76)	4.00 (0.83)	5.27 (6.20)	7.15 (6.51)	29.43 (41.68)	3.84 (3.39)
	Median [m]	-1.43 (-1.90)	-1.80 (-2.01)	-0.01 (-0.23)	3.78 (3.90)	3.99 (4.18)	5.51 (6.46)	1.54 (1.19)
	Std. Dev. [m]	46.72 (59.37)	47.45 (60.49)	18.91 (5.77)	10.33 (6.22)	28.35 (6.26)	65.25 (77.79)	6.88 (6.92)

358

https://doi.org/10.5194/tc-2019-250
Preprint. Discussion started: 27 November 2019

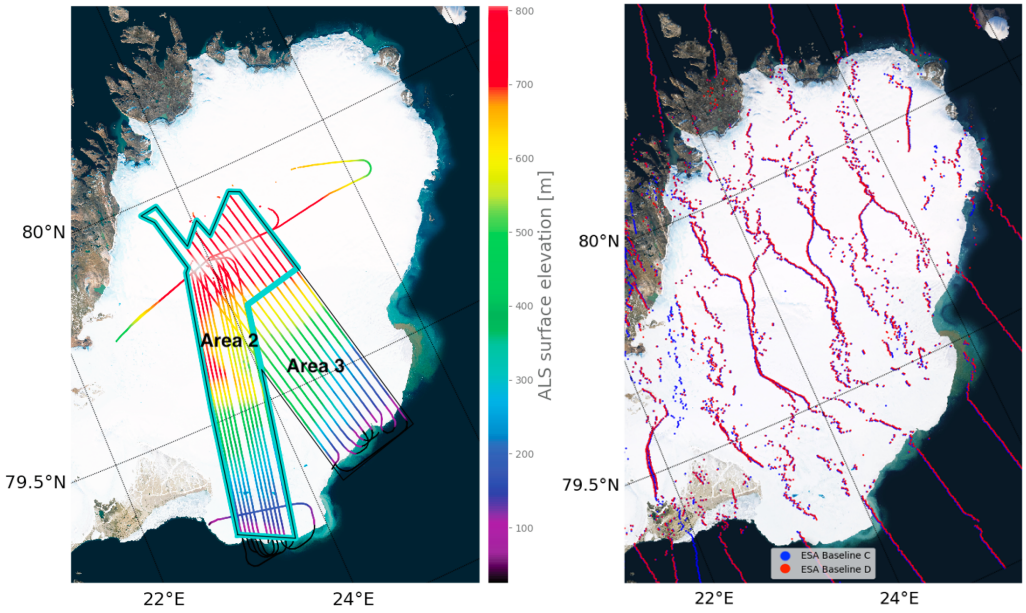

Figure 7 (Left panel) The surface elevation measured by the CryoVEx airborne laser scanning. The thin black line outlines the entire study area (Area 1); the two subareas are indicated in the figure. Here, Area 3 is covering the complex surface topography of the surging basin of the Austfonna ice sheet. (Right panel) the geolocations of the two ESA L2 Baselines. Map Data ©2019 Google

3.3 Sea Ice

3.3.1 Stack Peakiness Implementation

Statistics that describe the power of the stack in CryoSat were already present in the previous Baselines: Stack Kurtosis and Stack Standard Deviation (SSD). While performing an explorative study focused on distinguishing leads from ice surfaces, the adoption of a further parameter was proposed: the Stack Peakiness (SP). This compares the maximum power registered in the Range Integrated Power (RIP) with the power obtained from the other looks. It is also important to notice that this is different from the peakiness of the multi-looked waveform. The latter is influenced by all the looks ("multi-looked"), while the SP compares the influence of the look with the highest power (supposedly at nadir) with the looks taken at

https://doi.org/10.5194/tc-2019-250
Preprint. Discussion started: 27 November 2019

370 different viewing angles. The advantages in using the SP as a method of discriminating sea ice
371 floes from leads, instead of (or together with) Stack Kurtosis (SK) and SSD, are described in
372 Passaro et al., 2018. The evolution of the SP over a sea ice covered area is compared with the
373 SK and SSD stored in the official product (at the time of Baseline-C). The evolution of SP in
374 the lead areas are similar: a peak, which corresponds to the strongest return from the zero-look
375 angle compared to the other looks, is easily identifiable, but the lead returns also influence the
376 measurements nearby. The lead areas are also characterised by high kurtosis and low SSD, but
377 these two indices fail to univocally show a local maximum or minimum. The kurtosis presents
378 multiple peaks, which may be attributed to high power in non-zero look angles due to residual
379 side-lobe effects; the SSD, being based on a Gaussian fitting, is not able to distinguish subtle
380 differences in the power distribution of the very peaky RIP waveforms in the lead areas. The
381 exact formula to compute SP is reported in Passaro et al., 2018. The SP has now been included
382 in the new Baseline-D.
383

384 **3.3.2 CryoSat Baseline-D freeboard assessment**

385 Previous analyses carried out by the CryoSea-Nice ESA project (https://projects.along-
386 track.com/csn/) highlighted important over-estimations in the freeboard values of the ESA
387 CryoSat Baseline-C products relative to in-situ data. Following these conclusions,
388 modifications have been made to develop the new ESA CryoSat Baseline-D freeboard product.
389 We present here the first assessments of this updated version.

390 The freeboard maps in Figure 8 present the evolution between the two Baselines. They
391 demonstrate that the Baseline-D mean freeboard values have been significantly reduced. Aside
392 from a mean bias of about 10 cm (see map Figure 8c) the two solutions remain consistent with
393 each other. The Root Mean Square (RMS) in each 20 x 20 km^2 pixel, that can be considered as
394 an estimation of the noise level distribution, is about 15 cm for the two Baselines.

https://doi.org/10.5194/tc-2019-250
Preprint. Discussion started: 27 November 2019

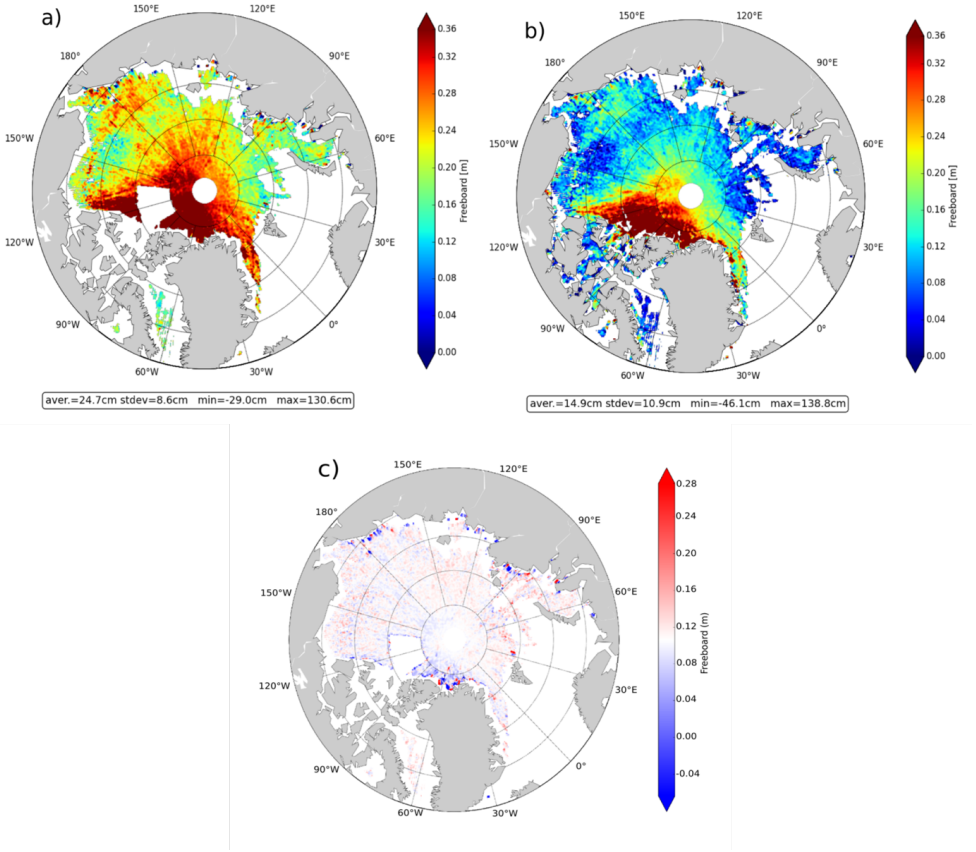

Figure 8: Monthly freeboard maps from the 10th March 2014 to the 11th April 2014 of the a) Baseline-C and b) Baseline-D versions. The third map c) presents the difference between the 2 previous maps (Baseline-C – Baseline-D). Note that the map c) colour bar is centred on 0,1 m to underline the mean bias deviation between the 2 versions.

Scatter comparisons with the Beaufort Gyre Exploration Project (BGEP, https://www.whoi.edu/beaufortgyre) and Operation IceBridge (OIB, Kurtz et al., 2013) in-situ measurements confirm the improvements of the Baseline-D freeboard product quality (see Figure 9). Relative to OIB, the Baseline-D freeboard mean bias is reduced by about 8 cm, which roughly corresponds to a 60% decrease. The BGEP data indicate a similar tendency with a mean draft bias lowered from 0.85 m to -0.14 m (mean draft is ~1 to 1.5 m). For the two in-

https://doi.org/10.5194/tc-2019-250
Preprint. Discussion started: 27 November 2019

406 situ datasets, the Root Mean Square Deviation (RMSD) is also well reduced from 14 cm to 11
407 cm for OIB and with a factor 2 for BGEP.

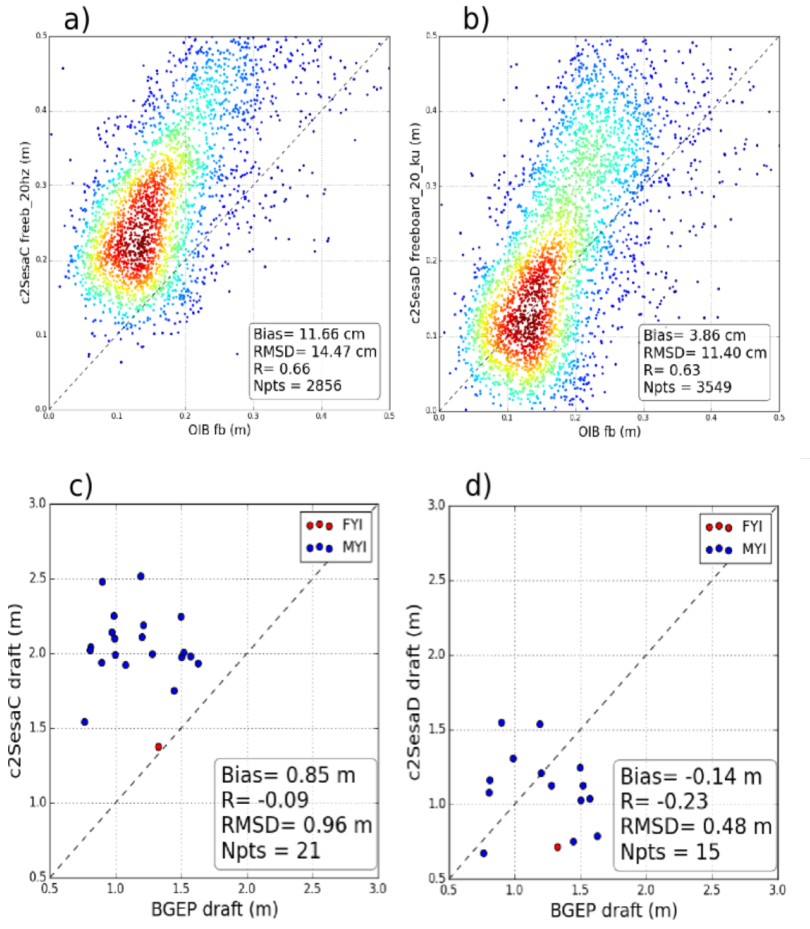

408

409 **Figure 9 Illustration of the Baseline-D product improvements by comparison with in-situ measurements. The first**
410 **two figures compare the 2014 Operation IceBridge (OIB) freeboard measurements with a) the Baseline-C and b) the**
411 **Baseline-D sea ice freeboard. The two following scatterplots compare the winter 2013/ 2014 Beaufort Gyre**
412 **Exploration Project (BGEP) sea ice freeboard converted to draft estimations with c) the Baseline-C and d) the**
413 **Baseline-D sea ice freeboards.**

414 Some additional comparisons have set the Baseline-D freeboard solution within the range
415 values of several recent estimations such as Ricker et al, 2014 and Guerreiro et al, 2017. All
416 together, these results demonstrate the positive improvements of the ESA Baseline-D freeboard

https://doi.org/10.5194/tc-2019-250
Preprint. Discussion started: 27 November 2019

417 product compared to the previous Baseline-C version. In addition, the improved phase
418 difference in SARIn mode had positive impacts on sea ice freeboard as presented in the next
419 section.

420

421 **3.3.3 Impact of SARIn phase difference on freeboard estimation**

422 Satellite altimetry has been used in the last 25 years to estimate sea ice thickness by directly
423 measuring the sea ice freeboard, i.e., the height of the sea ice above the local sea surface (Laxon
424 et al., 2003). The different physical characteristics of sea ice and leads, which provide the local
425 sea surface height, affect the shape and the power of the reflected radar pulses received by the
426 altimeter, allowing for surface discrimination. Retracking echoes coming from sea ice and
427 leads enables determination of the height of the sea ice and the sea level, respectively. Finally,
428 the freeboard height is obtained by subtracting the local sea surface height from the sea ice
429 elevations.
430 In sea ice covered regions, the accurate estimation of the sea surface height (SSH) highly
431 depends on the amount and spatial distribution of leads. A study by Armitage and Davidson,
432 2014, showed that the CryoSat SARIn acquisition mode can be used to obtain a more precise
433 SSH, as it enables processing of echoes that are usually discarded because of their ambiguity,
434 e.g., echoes dominated by the reflection from off-nadir leads. In fact, the phase information
435 available in the SARIn mode enables the across-track location on ground of the received echoes
436 to be determined and an off-nadir range correction (ONC) to be geometrically computed,
437 accounting for the range overestimation to off-nadir leads Laxon et al., 2003. The more precise
438 SSH obtained from SARIn measurements can reduce the average random uncertainty of
439 freeboard estimates (Di Bella et al., 2018).
440 Despite the overall reduction of the random freeboard uncertainty when including the phase
441 information, pan-Arctic sea ice freeboard estimates from CryoSat Baseline-C SAR/SARIn L1B

https://doi.org/10.5194/tc-2019-250
Preprint. Discussion started: 27 November 2019

442 products showed large negative freeboard heights at the boundary of the SARIn mode mask
443 (Figure 10a and Figure 10b). The analysis performed by Di Bella et al., 2019 attributed the
444 negative freeboard pattern observed in Figure 10a and Figure 10b to large values of ONC,
445 associated with inaccurate phase differences. The same study determined that the CAL4
446 correction, responsible to calibrate the phase difference between the signal received by the two
447 antennas (Fornari et al., 2014), was not applied at the beginning of a SARIn acquisition.
448 The Baseline-D SAR/SARIn IPF1 applies the CAL4 correction which is closest in time to the
449 19 bursts of the first SARIn acquisition, improving notably the phase difference and the
450 coherence at the retracking point. Looking at the Arctic freeboard estimates obtained from
451 Baseline-D SAR/SARIn L1B products in Figure 10c and Figure 10d, one can notice that the
452 negative freeboard pattern along the boundaries of the SARIn acquisition mask has
453 disappeared, highlighting a continuous freeboard spatial distribution throughout the Arctic
454 Ocean.
455 The Baseline-D IPF therefore improves the quality of the retrieved heights in areas up to ~12
456 km inside the SARIn acquisition mask, being beneficial not only for freeboard retrieval, but
457 for any application that exploits the phase information from SARIn L1B products.
458
459

https://doi.org/10.5194/tc-2019-250
Preprint. Discussion started: 27 November 2019

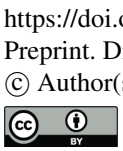

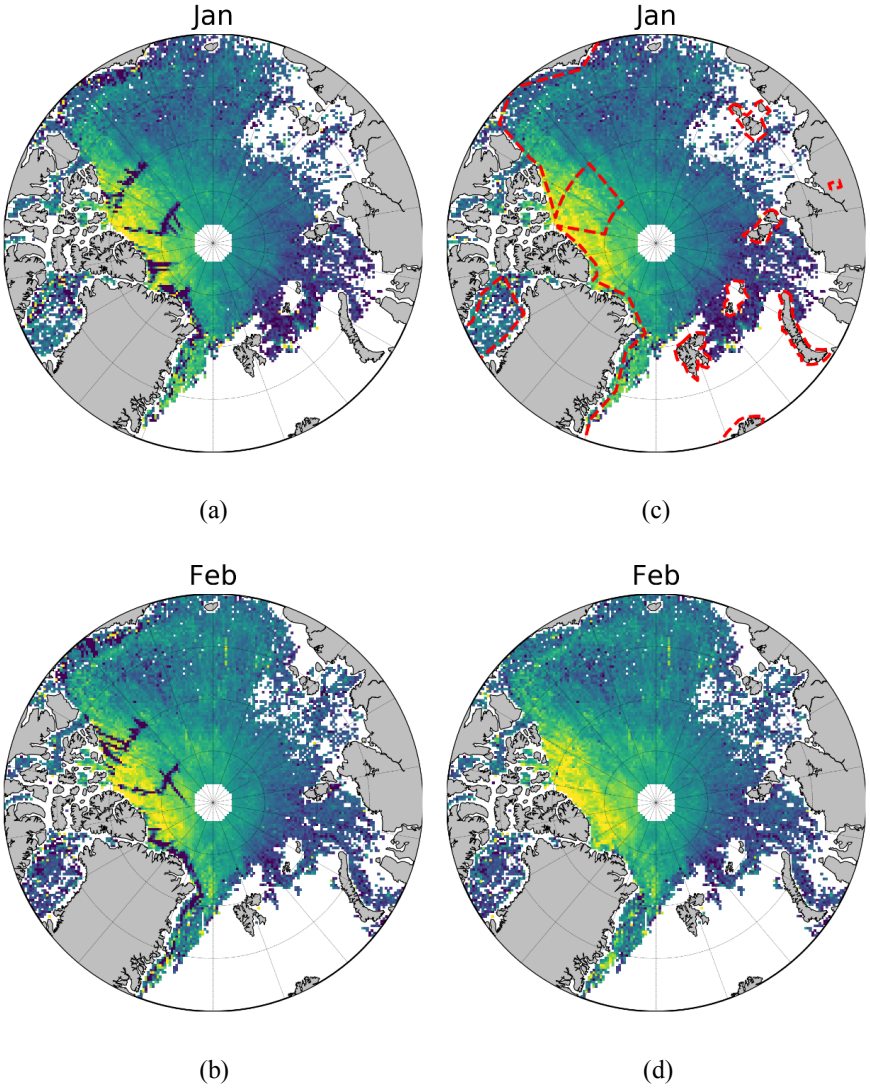

Figure 10 Gridded monthly freeboard from Baseline-C (a-b) and Baseline-D (c-d) L1b data for the period January/February 2014. The dashed red line in (c) represents the boundaries of the SARIn acquisition mask

3.3.4 Impact of algorithm evolution on sea ice thickness consistency

Operational L1B products generated by the CryoSat Baseline-C Ice processor (IPF1C) are a primary dataset for observing changes sea ice thickness in the northern hemisphere. Examples

https://doi.org/10.5194/tc-2019-250
Preprint. Discussion started: 27 November 2019

for the application of CryoSat L1B products in sea ice climate research are formalised climate data records such as those of the ESA Climate Change Initiative (CCI) (Paul et al., 2018, Hendricks et al., 2018b) and the Copernicus Climate Change Services (C3S) (Hendricks et al., 2018a, Hendricks et al., 2018b). In addition, several agencies and institutes generate sea ice data records based on the CryoSat L1B Baseline-C products (Tilling et al., 2018), AWI (Ricker et al., 2014, Kurtz et al. 2014, Kwok et al., 2015, Guerreiro et al., 2017). To estimate the impact of the algorithm evolution of the CryoSat Ice Processor to Baseline-D (IPF1D) on these sea ice data records, we compute sea ice thickness (SIT) for both IPF1C and IPF1D primary input datasets with an otherwise identical processing environment. The processing chain for this experiment has been developed at the Alfred Wegener Institute (AWI) (Ricker et al. 2014) and we utilise the most recent algorithm version 2.1 (Hendricks et al., 2019). The AWI processor is implemented in the python sea ice radar altimetry library along with the climate data records of the ESA CCI and C3S. Processing steps consist of a L2 processor for the estimation of sea ice freeboard and thickness at full along-track resolution and a L2 processor for mapping data on a space-time grid for a monthly period with a resolution of 25 km in the northern hemisphere. For a full description of the algorithm and processing steps we direct the reader to Hendricks et al., 2019. The CryoSat IPF1D input data is processed with the identical processor configuration as the current IPF1C based AWI reprocessed product line. The impact analysis is implemented for 5-month periods of the IPF1D test period (October – November 2013; February – April 2014) by evaluating pointwise differences (IPF1D – IPF1C) of gridded thickness from the two CryoSat primary input versions. Monthly statistics of sea ice thickness differences (ΔSIT) itemised for all grid cells in the northern hemisphere (ALL) as well as for the SAR and SIN modes of the altimeter is shown in Figure 11 and in Table 2. In addition, Figure 11 illustrates the regional distribution of ΔSIT exemplary for the monthly period of April 2014. The mean monthly thickness difference between IPF1D and IPF1C ($\overline{\Delta SIT}$) varies

https://doi.org/10.5194/tc-2019-250
Preprint. Discussion started: 27 November 2019

492 between -3 to -15 mm. Its magnitude is increasing over the winter season with highest values
493 in April, which we attribute to the increase of ice thicknesses over the winter period. However,
494 the radar mode plays an important role in the $\overline{\Delta SIT}$ result, as thickness measurements from
495 SAR data are significantly less impacted by the input version than SIN data. Regions with SIN
496 data therefore drive the magnitude and negative sign for hemispheric $\overline{\Delta SIT}$ (SAR: -5 to 9 mm,
497 SIN: -17 to -77 mm). On the map in Figure 11 this is particularly visible in the Wingham Box
498 (WHB), a region where CryoSat has operated in SIN mode from 2010 to 2014 and which has
499 a higher density of grid cells with negative ΔSIT. The magnitude of ΔSIT even for SIN is
500 however small compared to the SIT uncertainty for monthly gridded observations that are
501 mostly driven by the unknown variability of snow depth, surface roughness and sea ice density.
502 Average gridded SIT uncertainty in the AWI product for April 2014 is 0.64 m and we therefore
503 conclude that a maximum $\overline{\Delta SIT}$ of -0.015 m in the period of the TDS is insignificant for the
504 stability of sea ice data records. This impact analysis however does not provide any insights
505 into the specific algorithm changes that are causing the observed ΔSIT. We therefore speculate
506 that the change in power scaling for SIN data between IPF1C and IPF1D is the reason for the
507 larger impact on SIN data as the AWI surface type classification depends partly on total
508 waveform backscatter. An update to the surface type classification that includes the additional
509 stack peakiness information in IPF1D has the potential to further improve surface type
510 classification and consequently sea ice freeboard and thickness. The AWI processing chain is
511 based on the python sea ice radar altimetry processing library (pysiral). The source code is
512 available under a GNU General Public License v3.0 license
513 (https://github.com/shendric/pysiral). Reprocessed and operational sea ice thickness with
514 intermediate parameters for gridded and trajectory products of the AWI processing chain can
515 be accessed via the following ftp (ftp://ftp.awi.de/sea_ice/product/cryosat2/).

516

https://doi.org/10.5194/tc-2019-250
Preprint. Discussion started: 27 November 2019

517

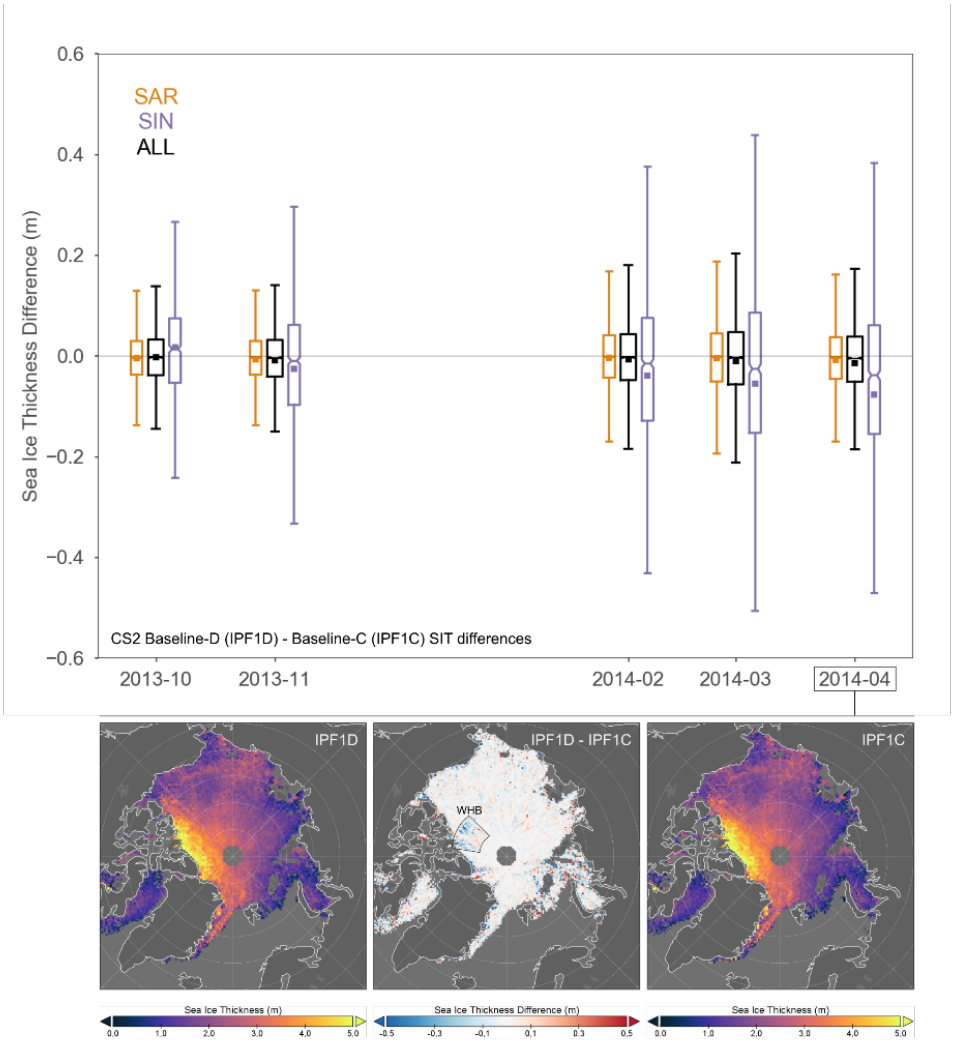

518

519 **Figure 11 [Upper panel] Time series of gridded monthly sea-ice thickness difference (ΔSIT) statistics for the AWI sea**
520 **ice processing chain based on the Baseline-D (IPF1D) test data set and Baseline-C (IPF1C) input. Differences**
521 **(Baseline-D minus Baseline-C) are colour-coded for all 25 km x 25km grid cells in northern hemisphere (ALL) and**
522 **separately for SAR and SIN input data. The inner boxed indicates the median difference with the confidence interval;**
523 **the square marker indicates mean difference ($\overline{\Delta SIT}$) and the vertical line the maximum ΔSIT range. [Lower panel]**
524 ***SIT* maps in April 2014 for IPF1D (left), IPF1C (right) and the IPF1D-IPF1C difference (center). The marked region**
525 **(WHB: Wingham Box) indicates an area where CryoSat operated in SIN mode.**

https://doi.org/10.5194/tc-2019-250
Preprint. Discussion started: 27 November 2019

526 **Table 2. Mean thickness difference ($\overline{\Delta SIT}$) and standard deviation ($\sigma_{\Delta SIT}$) for all monthly gridded fields during the**
527 **winter months (October – April) of the Baseline-D TDS. The statistics is broken down into a) all grid cells with data**
528 **coverage for both baselines b) SAR data and c) SIN data (highest ΔSIT values).**

	SAR+SIN (ALL)		SAR		SIN	
	$\overline{\Delta SIT}$ (m)	$\sigma_{\Delta SIT}$ (m)	$\overline{\Delta SIT}$ (m)	$\sigma_{\Delta SIT}$ (m)	$\overline{\Delta SIT}$ (m)	$\sigma_{\Delta SIT}$ (m)
2013-10	-0.003	0.12	-0.005	0.10	0.017	0.22
2013-11	-0.009	0.13	-0.007	0.11	-0.026	0.21
2014-02	-0.007	0.14	-0.004	0.12	-0.040	0.27
2014-03	-0.010	0.16	-0.005	0.13	-0.055	0.32
2014-04	-0.015	0.16	-0.009	0.14	-0.077	0.33

529

530

531 ### 3.3.5 Lead classification comparison between CryoSat Baseline-C and Baseline-D

532 Lead classification is essential for retrieving sea ice freeboard and thickness. Previously, the
533 threshold of parameters used for lead classification, such as Stack standard deviation (SSD)
534 and Pulse Peakiness (PP), was re-scaled from Baseline-B to Baseline-C. Lee et al., 2018
535 proposed a waveform mixture algorithm for lead classification which solely used a normalised
536 waveform. The results of lead classification are the same between Baseline-C and Baseline-D,
537 as illustrated in Figure 12, where the tracks are projected over MODIS imagery. This method
538 stably classifies leads without re-scaling parameters. The lead classification outside of the
539 MODIS image is the same as well. However, as only two example CryoSat products are used
540 for the comparison, this does not guarantee that the results of lead classification are consistent
541 across the entire dataset. The stable lead classification brings a robust retrieval of sea ice
542 freeboard and thickness.

https://doi.org/10.5194/tc-2019-250
Preprint. Discussion started: 27 November 2019

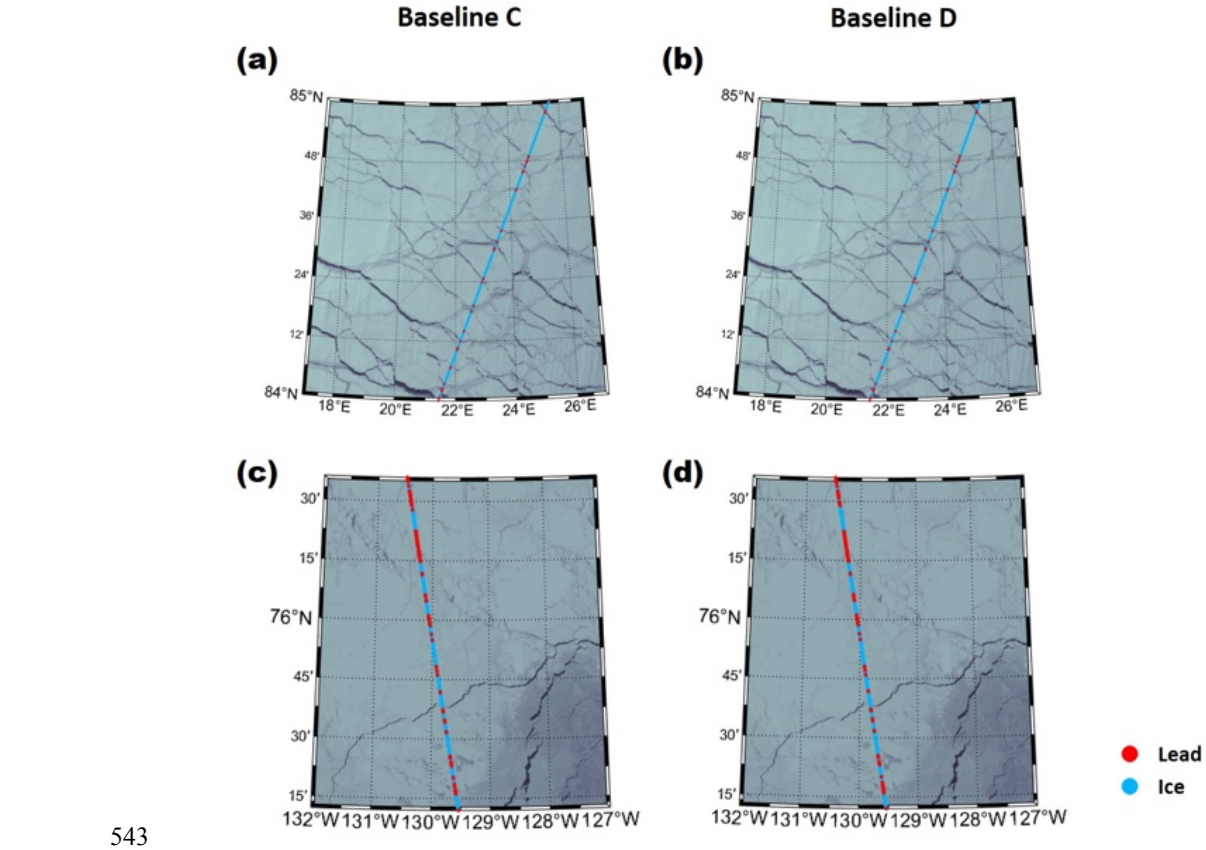

Figure 12 Red dots represent lead, light blue dots represent ice. (a, b) the MODIS images are from 17 Apr. 2014 22:10 (UTC); CryoSat passes over after 21 minutes. (c, d) the MODIS images are from 17 Oct. 2013 22:10 (UTC); CryoSat passes over after 5 minutes.

3.4 Inland Waters

Whilst CryoSat was initially designed to measure the changes in the thickness of polar sea ice, the elevation of the ice sheets and mountain glaciers, the mission has gone above and beyond its original objectives. Scientists have discovered that the CryoSat's altimeter has the capability to map sea level close to the coast and to profile land surfaces and inland water targets such as small lakes, rivers and their intricate tributaries (Schneider et al., 2017). In this respect, to evaluate the new CryoSat Baseline-D TDS for lake level estimation two study areas were

https://doi.org/10.5194/tc-2019-250
Preprint. Discussion started: 27 November 2019

555 selected: Sweden which is covered by SAR mode and the Tibetan Plateau which is covered by
556 SARIn mode. Both areas have a dense concentration of lakes with a large range of sizes. In
557 both cases the period September to November 2013 is studied. The evaluated products are the
558 L2 products (SIR_SAR_L2 and SIR_SIN_L2) for Baseline-C and Baseline-D. The surface
559 elevations are extracted using a water mask and referenced to the EGM 2008 geoid model. In
560 the evaluation the standard deviation of the individual water level measurements is estimated
561 for each track and as a summary measure the median of the distribution of standard deviations
562 (MSD) is used. The standard deviation is estimated using a robust error distribution consisting
563 of 70% Gaussian and 30% Cauchy (Nielsen et al, 2015). Furthermore, the percentage of "good
564 observations" is calculated. Here a good measurement is defined as a measurement within one
565 meter of the estimated track mean. To get solid statistics only tracks with 15 or more
566 measurements are used in the analysis. For comparison the analysis was conducted for both
567 Baseline-C and Baseline-D. For the Swedish area the analysis is based on 26 tracks covering
568 15 lakes with areas ranging from 29 to 3559 km^2. It is found that the MSDs are 7.3 cm and 7.1
569 cm for Baseline-C and Baseline-D, respectively. With respect to the percentage of "good
570 observations", a convincing increase is observed for Baseline-D (Figure 13). The larger number
571 of valid measurements reduces the error of the mean lake level for each track, which is used in
572 the construction of water level time series. 104 tracks covering 57 lakes with areas between
573 101 and 2407 km^2 are investigated on the Tibetan Plateau. It is found that the MSDs are 19.2
574 cm and 18.8 cm for Baseline-C and Baseline-D, respectfully. Furthermore, the approximately
575 60 m offset in the surface elevation that is present in Baseline-C is eliminated in Baseline-D.
576 For Baseline-D a slight increase in the percentage of "good observations", generally around 5-
577 10 % for most lakes, is observed.

https://doi.org/10.5194/tc-2019-250
Preprint. Discussion started: 27 November 2019

The Cryosphere
Discussions
Open Access
EGU

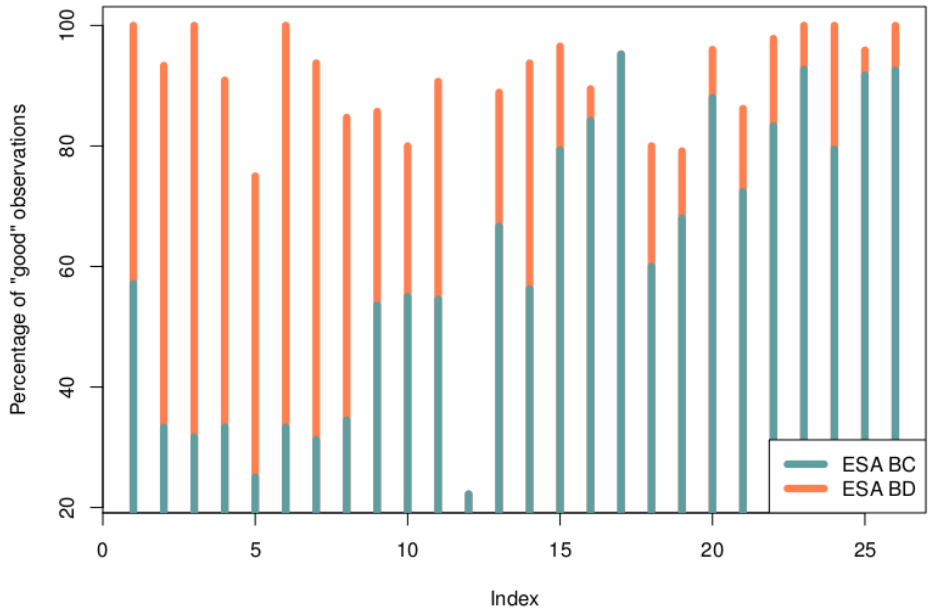

578

579 **Figure 13 The percentage of "good measurements" for Baseline-C (blueish) and Baseline-D (coral) based on 26 tracks**

580 **covering 15 Swedish lakes.**

581

https://doi.org/10.5194/tc-2019-250
Preprint. Discussion started: 27 November 2019

4 Conclusions

In conclusion, validation activities presented in this paper confirm that the new Baseline-D Ice L1B and L2 data show significant improvements with respect to Baseline-C over all surface types while the migration to netCDF make these new products more user-friendly than the previous EEF products. The assessment of a 6-month TDS by multi-thematic CryoSat expert users was instrumental in confirming data quality and providing an endorsement from the scientific community before the transfer of the Baseline-D Ice Processors to operational production on 27th May 2019. The Baseline-D algorithms show significant improvements over all kinds of surfaces. Most notably, freeboard is less noisy, no longer overestimated and scatter comparisons with in-situ measurements confirm the improvements of the Baseline-D freeboard product quality with a reduction of mean bias by about 8 cm, which roughly corresponds to a 60% decrease with respect to Baseline-C. For the two in-situ datasets considered (OIB and BGEP) the RMSD is also well reduced from 14 cm to 11 cm for OIB and by a factor 2 for BGEP. In addition, freeboard no longer shows discontinuities at SAR/SARIn interfaces. Over land ice, the main improvements are due to the increased accuracy in the roll angle. This has provided better results with respect to previous baseline when comparing the data to a reference DEM over the Austfonna ice cap region, and improved the ascending and descending crossover statistics from 1.9 m to 0.1 m. Inland water users also reported significant improvements including a reduction in previously observed measurement outliers and an increased percentage of "good observations", generally around 5-10% for most lakes. Overall, this new CryoSat processing Baseline-D will maximize the uptake and use of CryoSat data by scientific users since it offers improved capability for monitoring the complex and multi-scale changes in the thickness of sea ice, the elevation of ice sheets and mountain glaciers and their effect on climate change.

https://doi.org/10.5194/tc-2019-250
Preprint. Discussion started: 27 November 2019

606 **5 References**

607

608 Armitage, T. W. K. and Davidson, M. W. J.: Using the Interferometric Capabilities of the ESA
609 CryoSat-2 Mission to Improve the Accuracy of Sea Ice Freeboard Retrievals, IEEE
610 Transactions on Geoscience and Remote Sensing, vol. 52, no. 1, pp. 529–536, 2014.

611

612 Bouffard, J., Naeije, M., Banks, C., Calafat, F. M., Cipollini, P., Snaith, H. M., Webb, E., Hall,
613 A., Mannan, R., Féménias, P. and Parrinello, T.: CryoSat ocean product quality status and
614 future evolution, Advances in Space Research, Volume 62, Issue 6, , Pages 1549-1563,
615 ISSN 0273-1177, https://doi.org/10.1016/j.asr.2017.11.043, 2018a.

616

617 Bouffard, J., Webb, E., Scagliola, M, Garcia-Mondéjar, A., Baker, S., Brockley, D., Gaudelli,
618 J., Muir, A., Hall, A., Mannan, R., Roca, M., Fornari, M., Féménias, P. and Parrinello, T.:
619 CryoSat instrument performance and ice product quality status, Advances in Space
620 Research, Volume 62, Issue 6, Pages 1526-1548, ISSN 0273-1177,
621 https://doi.org/10.1016/j.asr.2017.11.024, 2018b.

622

623 Di Bella, A., Skourup, H., Bouffard, J. and Parrinello, T.: Uncertainty reduction of arctic sea
624 ice freeboard from CryoSat-2 interferometric mode Advances in Space Research, vol. 62,
625 no. 6, pp. 1251 – 1264, the CryoSat Satellite Altimetry Mission: Eight Years of Scientific
626 Exploitation, 2018.

627

628 Di Bella, A., Scagliola, M., Maestri, L., Skourup, H., and Forsberg, R.: Improving CryoSat
629 SARIn L1b products to account for inaccurate phase difference: impact on sea ice freeboard
630 retrieval, IEEE Geoscience and Remote Sensing Letters, 10.1109/LGRS.2019.2919946,
631 2019.

Dunse, T., Schuler, T. V., Hagen, J. O., and Reijmer, C. H.: Seasonal speed-up of two outlet glaciers of Austfonna, Svalbard, inferred from continuous GPS measurements, The Cryosphere, 6, 453-466, https://doi.org/10.5194/tc-6-453-2012, 2012.

Dunse, T., Schellenberger, T., Hagen, J. O., Kääb, A., Schuler, T. V., and Reijmer, C. H.: Glacier-surge mechanisms promoted by a hydro-thermodynamic feedback to summer melt, The Cryosphere, 9, 197-215, https://doi.org/10.5194/tc-9-197-2015, 2015.

Fornari, M., Scagliola, M., Tagliani, N., Parrinello, T. and Mondejar, A. G.: CryoSat: Siral calibration and performance, IEEE Geoscience and Remote Sensing Symposium, July 2014, pp. 702–705, 2014.

Gourmelen, N., Goldberg, D. N., Snow, K., Henley, S. F., Bingham, R. G., Kimura, S., Hogg, E., Sheperd, A., Mouginot, J., Lenaerts, J., Ligtenberg, S. R. M. and Berg, W. J.: Channelized melting drives thinning under a rapidly melting Antarctic ice shelf, Geophysical Research Letters, 44, 9796– 9804, https://doi.org/10.1002/2017GL074929, 2017.

Gourmelen, N., Escorihuela, M.J., Shepherd, A., Foresta, L., Muir, A., Garcia-Mondejar, A., Roca, M., Baker, S. G., Drinkwater, M. R.: CryoSat-2 swath interferometric altimetry for mapping ice elevation and elevation change, Advances in Space Research, Volume 62, Issue 6, 2018, Pages 1226-1242, ISSN 0273-1177, https://doi.org/10.1016/j.asr.2017.11.014.

https://doi.org/10.5194/tc-2019-250
Preprint. Discussion started: 27 November 2019

659 Gray, L., Burgess, D., Copland, L., Cullen, R., Galin, N., Hawley, R., and Helm, V.:
660 Interferometric swath processing of CryoSat data for glacial ice topography. The
661 Cryosphere, 7, 1857–1867, 2013.
662
663 Gray, L., Burgess, D., Copland, L., Demuth, M. N., Dunse, T., Langley, K., and Schuler, T.
664 V.: CryoSat-2 delivers monthly and inter-annual surface elevation change for Arctic ice
665 caps, The Cryosphere, 9, 1895-1913, https://doi.org/10.5194/tc-9-1895-2015, 2015.
666
667 Gray, L., Burgess, D., Copland, L., Dunse, T., Langley, K., and Moholdt, G.: A revised
668 calibration of the interferometric mode of the CryoSat-2 radar altimeter improves ice height
669 and height change measurements in western Greenland, The Cryosphere, 11, 1041-1058,
670 https://doi.org/10.5194/tc-11-1041-2017, 2017.
671
672
673 Guerreiro, K., Fleury, S., Zakharova, E., Kouraev, A., Rémy, F., and Maisongrande, P.:
674 Comparison of CryoSat-2 and ENVISAT radar freeboard over Arctic sea ice: toward an
675 improved Envisat freeboard retrieval, The Cryosphere, 11, 2059-2073,
676 https://doi.org/10.5194/tc-11-2059-2017, 2017.
677
678 Helm, V., Humbert, A., and Miller, H.: Elevation and elevation change of Greenland and
679 Antarctica derived from CryoSat-2, The Cryosphere, 8, 1539-1559,
680 https://doi.org/10.5194/tc-8-1539-2014, 2014.
681
682
683 Hendricks, S., Paul, S. and Rinne, E.: ESA Sea Ice Climate Change Initiative (Sea_Ice_cci):
684 Northern hemisphere sea ice thickness from the CryoSat-2 satellite on a monthly grid (L3C),

https://doi.org/10.5194/tc-2019-250
Preprint. Discussion started: 27 November 2019

685 v2.0. Centre for Environmental Data Analysis,
686 http://dx.doi.org/10.5285/ff79d140824f42dd92b204b4f1e9e7c2, 2018a.
687
688
689 Hendricks S. and Ricker R.: Sea Ice Thickness: Product User Guide and Specification,
690 Copernicus Climate Change Services (C3S), Technical Report version 1.1 (Ref:
691 C3S_D312a_lot1.3.3.3-v1_201805_PUGS_v1.1), http://datastore.copernicus-
692 climate.eu/c3s/published-forms/c3sprod/satellite-sea-ice/product-user-guide-sea-ice-
693 thickness.pdf, 2018b.
694
695 Hendricks, S. and Ricker, R.: Product User Guide & Algorithm Specification: AWI CryoSat-2
696 Sea Ice Thickness (version 2.1), Technical Report, hdl:10013/epic.7dacf2fe-bead-4a1b-
697 a266-c4fdd022877f, https://epic.awi.de/id/eprint/49542/, 2019.
698
699 Kurtz, N. T., Farrell, S. L., Studinger, M., Galin, N., Harbeck, J. P., Lindsay, R., Onana, V. D.,
700 Panzer, B. and Sonntag, J. G.: Sea ice thickness, freeboard, and snow depth products from
701 Operation IceBridge airborne data. The Cryosphere, 7, 1035-1056, 2013.
702
703 Kurtz, N. T., Galin, N., and Studinger, M.: An improved CryoSat-2 sea ice freeboard retrieval
704 algorithm through the use of waveform fitting, The Cryosphere, 8, 1217-1237,
705 https://doi.org/10.5194/tc-8-1217-2014, 2014.
706
707 Kwok R. and Cunningham, G. F.: Variability of Arctic sea ice thickness and volume from
708 CryoSat-2, Phil. Trans. R. Soc. A 2015 37320140157; DOI: 10.1098/rsta.2014.0157, 2015.
709

https://doi.org/10.5194/tc-2019-250
Preprint. Discussion started: 27 November 2019

710 Laxon, S., Peacock, N. and Smith, D.: High interannual variability of sea ice thickness in the
711 Arctic region, Nature, vol. 425, no. 6961, pp. 947–950, 2003.
712
713 Lee, S., Kim, H. C., and Im, J.: Arctic lead detection using a waveform mixture algorithm
714 from CryoSat-2 data. The Cryosphere, 12(5), 1665-1679, 2018
715
716 McMillan, M., A. Shepherd, A. Sundal, K. Briggs, A. Muir, A. Ridout, A. Hogg, and D.
717 Wingham: Increased ice losses from Antarctica detected by CryoSat-2, Geophysical
718 Research Letters, 41, 3899–3905,doi:10.1002/2014GL060111, 2014.
719
720 Nielsen, K., Stenseng, L., Andersen, B., Villadsen, H. and Knudsen, P.: Validation of CryoSat-
721 2 SAR mode based lake levels. Remote Sensing of Environment. 171. 162-170.
722 10.1016/j.rse.2015.10.023, 2015.
723
724 Nilsson, J., Vallelonga, P., Simonsen, S., Sørensen, L., Forsberg, R., Dahl-Jensen, D.,
725 Hirabayashi, M., Goto-Azuma, K., Hvidberg, C., Kjær, H., and Satow, K.: Greenland 2012
726 melt event effects on CryoSat-2 radar altimetry: Effect of Greenland melt on CryoSat-2.
727 Geophysical Research Letters. 42. 10.1002/2015GL063296, 2015.
728
729 Nilsson, J., Gardner, A., Sandberg Sørensen, L., and Forsberg, R.: Improved retrieval of land
730 ice topography from CryoSat-2 data and its impact for volume-change estimation of the
731 Greenland Ice Sheet, The Cryosphere, 10, 2953-2969, https://doi.org/10.5194/tc-10-2953-
732 2016.
733

https://doi.org/10.5194/tc-2019-250
Preprint. Discussion started: 27 November 2019

734 Passaro, M., Müller, F. and Dettmering, D.: Lead detection using CryoSat-2 delay-doppler
735 processing and Sentinel-1 SAR images, Advances in Space Research, Volume 62, Issue 6,
736 Pages 1610-1625, 2018.
737
738 Paul, S., Hendricks, S., Ricker, R., Kern, S. and Rinne, E.: Empirical parametrization of Envisat
739 freeboard retrieval of Arctic and Antarctic sea ice based on CryoSat-2: progress in the ESA
740 Climate Change Initiative, The Cryosphere, 12, 2437-2460, https://doi.org/10.5194/tc-12-
741 2437-2018, 2018.
742
743 Ricker, R., Hendricks, S., Helm, V., Skourup, H., and Davidson, M.: Sensitivity of CryoSat-2
744 Arctic sea-ice freeboard and thickness on radar-waveform interpretation. The Cryosphere,
745 8(4), 1607-1622, 2014.
746
747 Roemer, S., Legrésy, B., Horwath, M. and Dietrich, R.: Refined analysis of radar altimetry data
748 applied to the region of the subglacial Lake Vostok/Antarctica. Remote Sensing of
749 Environment. 106. 269-284. 10.1016/j.rse.2006.02.026, 2007.
750
751
752 Sandberg Sørensen, L. , Simonsen, S. , Langley, K. , Gray, L. , Helm, V. , Nilsson, J. ,
753 Stenseng, L. , Skourup, H. , Forsberg, R. and Davidson, M.: Validation of CryoSat-2 SARIn
754 Data over Austfonna Ice Cap Using Airborne Laser Scanner Measurements , Remote
755 Sensing, 10 (9), p. 1354 . doi: 10.3390/rs10091354, 2018.
756
757
758 Scagliola, M. and Fornari, M.: Quality improvements in SAR/SARIn BaselineC Level1b
759 products, C2-TN-ARS-GS-5154, ISSUE: 1.3 , 9 February 2015, available at
760 https://wiki.services.eoportal.org/tiki-

761 download_wiki_attachment.php?attId=3555&page=CryoSat%20Technical%20Notes&do
762 wnload=y
763
764 Scagliola, M., Fornari, M. and Tagliani, N.: Pitch Estimation for CryoSat by Analysis of Stacks
765 of Single-Look Echoes, *IEEE Geoscience and Remote Sensing Letters*, vol. 12, no. 7, pp.
766 1561-1565, 2015.
767
768 Scagliola, M., Fornari, M., Bouffard, J. and Parrinello, T.: The CryoSat interferometer: End-
769 to-end calibration and achievable performance, Advances in Space Research, Volume 62,
770 Issue 6, 1516-1525, 2018.
771
772 Schneider, R., Godiksen, P. N., Villadsen, H., Madsen, H., and Bauer-Gottwein, P.:
773 Application of CryoSat-2 altimetry data for river analysis and modelling, Hydrol. Earth
774 Syst. Sci., 21, 751–764, https://doi.org/10.5194/hess-21-751-2017, 2017.
775
776 Schröder, L., Horwath, M., Dietrich, R., Helm, V., van den Broeke, M. R., and Ligtenberg, S.
777 R. M.: Four decades of Antarctic surface elevation changes from multi-mission satellite
778 altimetry, The Cryosphere, 13, 427-449, https://doi.org/10.5194/tc-13-427-2019, 2019.
779
780 Simonsen, S. B. and Sørensen, L. S.: Implications of changing scattering properties on
781 Greenland ice sheet volume change from CryoSat-2 altimetry, Remote Sensing of
782 Environment, Volume 190, 207-216, ISSN 0034-4257,
783 https://doi.org/10.1016/j.rse.2016.12.012, 2017.
784
785 Skourup, H. ; Simonsen, S. B. ; Sørensen, L. Sandberg ; Helm, V. ; Hvidegaard, S. M. ; Di
786 Bella, A. ; Forsberg, R. / ESA CryoVEx/EU ICE-ARC 2016 - Airborne field campaign

https://doi.org/10.5194/tc-2019-250
Preprint. Discussion started: 27 November 2019

with ASIRAS radar and laser scanner over Austfonna, Fram Strait and the Wandel Sea. Kgs. Lyngby : Technical University of Denmark, 2018. 70 p.

Tilling Rachel L., Ridout, A., and Shepherd, A.: Estimating Arctic sea ice thickness and volume using CryoSat-2 radar altimeter data, Advances in Space Research, Volume 62, Issue 6, https://doi.org/10.1016/j.asr.2017.10.051, 2018.

Villadsen, H., Andersen, O. B., Stenseng, L., Nielsen, K. and Knudsen, P.: CryoSat-2 altimetry for river level monitoring — Evaluation in the Ganges–Brahmaputra River basin, Remote Sensing of Environment, Volume 168, 80-89, ISSN 0034-4257, https://doi.org/10.1016/j.rse.2015.05.025, 2015.